Extrinsic and intrinsic factors governing the electrochemical oxidation of propylene in aqueous solutions

Tae Gyu Yun[1], Boqiang Chen[1], Sarah Wells[1], Younghwan Lim[2], Jun Seop Kim[2], Ana Guilherme Buzanich[3], Martin Radtke[3], Matthias M. Waegele[1], Marcel Risch[4], and Alexis Grimaud[1]*

[1]Department of Chemistry, Boston College, MA 02467, United States

[2]Department of Materials Science and Engineering, Korea Advanced Institute of Science and Technology, Daejeon 34141, Korea

[3]Bundesanstalt für Materialforschung und -prüfung (BAM), Richard Willstatter Str. 11, 12205 Berlin, Germany

[4]Nachwuchsgruppe Gestaltung des Sauerstoffentwicklungsmechanismus, Helmholtz–Zentrum Berlin für Materialien und Energie GmbH, Hahn-Meitner Platz 1, Berlin 14109, Germany

*Corresponding author: alexis.grimaud@bc.edu

Abstract

The electrochemical synthesis of commodity chemicals, such as epoxides and glycols, offers a sustainable alternative to conventional methods that involve hazardous chemicals. Efforts to improve the yield and selectivity of propylene oxidation using Pd-based catalysts have shown to be highly sensitive on applied potential, pH and electrochemical cell design. Record efficiencies and yields were obtained by substitution of PdO by 4*d* or 5*d* transition metals, including Pt, with thus far little rationale regarding the origin for the improvement. Through electrochemical analysis, scanning transmission electron microscopy, X-ray absorption spectroscopy, and surface-enhanced infrared absorption spectroscopy, we investigated the mechanism of propylene oxidation on Pd-based catalysts. We demonstrate that adsorbates forming on PdO, where Pd adopts a square-planar coordination [PdO_4], differ from that forming on the surface of oxidized metallic Pd catalysts, with an oxo intermediate mediating propylene oxidation on PdO. We further show that Pt substitution in PdO does not modify this oxo intermediate. Varying pH, we found that the onset for propylene oxidation is pH-independent, indicating the potential-determining step where the proton is not involved in and similar reaction pathway in acidic and near-neutral conditions. Finally, our work undoubtedly demonstrate that, high Faradic efficiency towards propylene glycol and propylene oxide formation, such as those previously reported in the literature, can be achieved by electrode engineering means and mastery of mass transport and local pH. Notably, we achieved ≈100% faradaic efficiency for propylene glycol at 1.7 V *vs.* RHE in acidic media using Pt-substituted PdO catalyst loaded onto a gas diffusion electrode.

Introduction

The electrochemical synthesis of commodity chemicals, including those formed by the reduction of CO_2 (alcohols, etc.)[1,2] and N_2 (ammonia, etc)[3,4], or the anodic epoxidation of olefin[5–20], has attracted significant attention in recent years. When powered by renewables, electrosynthesis routes can provide a sustainable alternative to more energy intensive reactions requiring high-temperature and/or high-pressure. A wealth of electrochemical reactions has thus been developed, allowing the forging of useful chemical bonds and functional groups, and making possible the production of natural compounds for which chemical synthesis has no practical solution. However, to compete with well-established processes, selectivity and yield must be perfectly controlled.[21]

Propylene is a highly versatile chemical yielding various products as function of pH and the applied potential (Figure S1). Among these, propylene glycol (PG) and propylene oxide (PO) stand out due to their wide range of applications in the production of polymers, pharmaceuticals, and antifreezing applications.[22] PO is typically produced by the chlorohydrin process or a hydrogen peroxide-based method, while PG is synthesized by the hydrolysis of PO.[22–25] These conventional processes require hazardous chemicals, including $Cl_{2(g)}$ and $H_2O_{2(l)}$, and high temperatures. [22,25–27] In contrast, the electrochemical oxidation of propylene using water as the sole oxygen source has been increasingly studied as a cleaner alternative that avoids the formation of hazardous by-products.[10–20] However, poor selectivity remains a significant challenge due to competition with the oxygen evolution reaction (OER) at high anodic potentials over 1.4 V *vs.* RHE.

Pd-based catalysts, known to be poor OER catalysts, have been widely studied for their ability to selectivity oxidize propylene. Oxidation of allylic carbon from propylene occurs at low potentials (below 1.2 V *vs.* RHE) in 0.1 M $HClO_4$ on Pd metal surface,[13] resulting in the

formation of acrolein, acrylic acid, and allyl alcohol. In contrast, at potentials exceeding 1.2 V *vs.* RHE, the vinyl group is primarily oxidized, leading to the production of PG with a Faradaic efficiency (FE) of 13%. X-ray absorption spectroscopy (XAS) and density functional theory (DFT) calculations revealed that PG forms on the oxide monolayer forming on the surface of Pd in anodic conditions.[17,18] Using attenuated total reflectance-Fourier transform infrared (ATR-FTIR) spectroscopy, it was later demonstrated that the vinyl carbon adsorbs onto PdO surface and subsequently reacts with lattice oxygen to produce PG with an FE of 25% at 1.4 V *vs.* RHE.[12] The mechanism by which propylene oxidize on Pd-based catalysts is therefore well understood at potentials less anodic than the OER onset potential, while at potentials greater than 1.4 V *vs.* RHE, where high current densities can be achieved, the FE remains limited.

Due to its tendency to rapidly hydrolyze into PG in acidic solutions, PO can only be detected/produced under near-neutral conditions unlike PG which is formed readily in acidic conditions. Recently, Pt-substituted PdO catalyst was reported to achieve ≈ 60% FE in both an hybrid H_2O/acetonitrile electrolyte and a phosphate buffer solution (PBS, pH 6).[11] Similarly, the formation of PG was observed under near-neutral solutions with a 75% FE on Rh-doped Pd, alongside a small amount of PO.[15] Using operando Raman spectroscopy coupled with DFT calculations, the authors proposed that propylene is directly oxidized into PG following the formation of an hydroxy intermediate. Nevertheless, PG was also observed under strongly acidic conditions, where the formation of a hydroxide layer is unlikely, and when using unbuffered solutions,[28] making it possible that PO is initially produced before being hydrolyzed to PG. Despite its fast hydrolysis, report of PO production in acidic solution was made, with nonetheless the necessity to use a specialized electrochemical cell setup in which PO is separated from the acidic medium and transferred into an organic solvent.[19,20] Hence, chemicals produced by the oxidation of propylene vary significantly depending on the pH of the solution and the design of the electrochemical cell, with thus far no precise design rationale for the latter.

Additionally, controversy exists regarding the mechanism by which PG forms, either via the hydrolysis of PO electrochemically generated, suggesting a shared oxidation mechanism and intermediates, or through a distinct, independent mechanism during propylene oxidation. Finally, the role of substitution in the propylene oxidation mechanism and enhanced performance of PdO remains poorly understood.

In pursuit of design principles to enhance the efficiency of propylene oxidation reactions, we investigate in this work how factors including pH, formation of oxygenated surface intermediates and cell design impacts the yield and selectivity of Pd-based catalysts towards production of PG and PO. For that, we compared metallic Pd catalyst with PdO., while results obtained with Pt-substituted PdO were compared with that collected for PdO and Pt to reveal the effect of Pt substitution. By comparing the electrochemical oxidation mechanism of propylene in acidic media, we illuminate using surface enhanced infrared absorption spectroscopy (SEIRAS) that the stark difference in selectivity and activity for oxidized Pd surface and PdO is nested into the presence of an oxo intermediate forming on square planar geometry only observed for PdO. Furthermore, we reveal that Pt-substitution does not result in a change in reaction intermediates. Instead, by varying pH and conducting electrolysis experiments using different electrochemical cell designs, we demonstrate that high FE previously reported for Pd-based catalysts originate from extrinsic factors, rather than intrinsic properties. Indeed, our results revealed that Pt-doped PdO can achieve 100% FE for PG in 0.1 M $HClO_4$ and 50% FE for PO in PBS using hydrophobic coatings and a gas diffusion configuration. Overall, our study points that careful design and environmental conditions can significantly influence experimental outcomes.

Result and discussion

Characterization of electrocatalysts. Proton nuclear magnetic resonance (^{1}H-NMR) was first used to confirm that PO is fully converted into PG in acidic conditions (pH < 3), while at near-neutral conditions previously reported to produce PO, *i.e.* pH 4−7, PO is found to partially and almost fully convert into PG after 3 days and 3 weeks, respectively, and that even at pH 7 (Figure 1 and Figure S2). As a result, electrochemical oxidation of propylene must be conducted under near-neutral conditions to observed the production of PO, and the PO must be collected promptly to minimize conversion to PG.

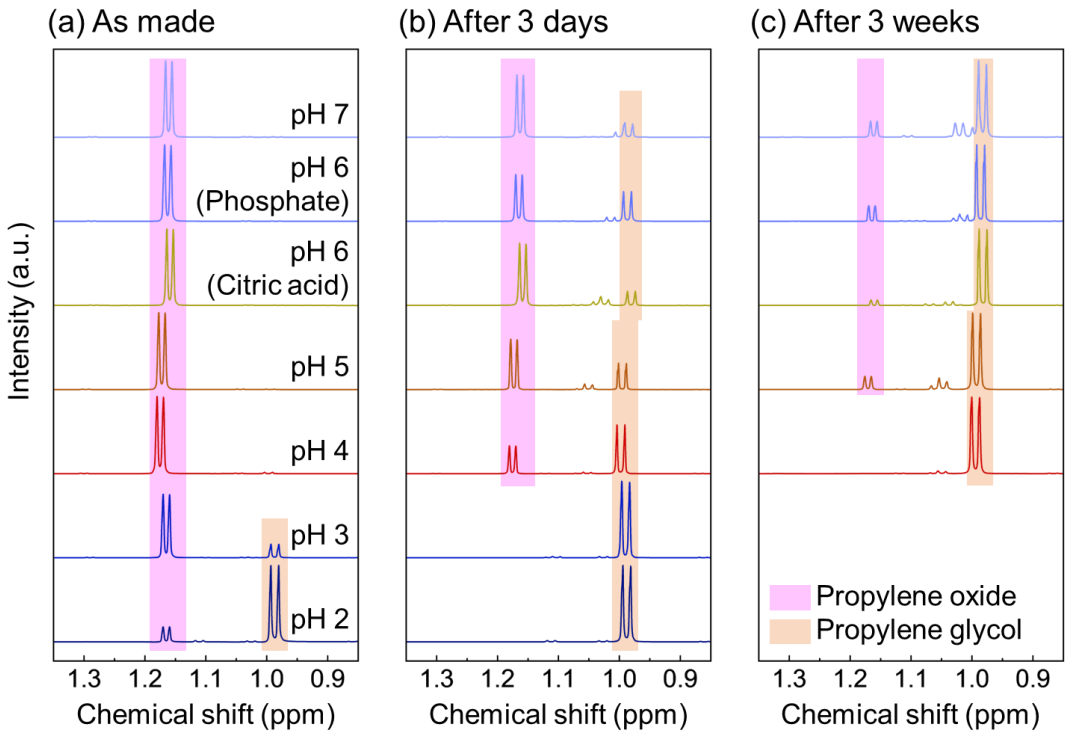

Figure 1. Chemical stability of PO. ^{1}H-NMR spectra of PO containing solutions with pH ranging from 2 to 7. The ^{1}H-NMR spectra were taken immediately after the sample preparation (a), after 3 days (b), and after 3 weeks (c). Small peaks aside to PG are from residual ethanol and isopropanol after cleaning NMR tubes.

Having shown that PO hydrolysis is complete and almost spontaneous in acidic conditions, we

then focused our efforts on screening the effect of coordination, oxidation state and Pt-substitution on the yield and rate for propylene oxidation in both acidic and neutral conditions and compared these results with those obtained for IrO_2, considered as a good OER catalyst. Pd, Pt, PdO, and IrO_2 nanoparticles were synthesized using the polyol method.[29–31] X-ray diffractograms indicate the formation of the desired phases, with some minor secondary phases (Figure 2a−d). STEM high-angle annular dark-field (HAADF) images (Figure 2e−h) reveal a well-defined surface with clear atomic columns. Metallic catalysts (Pd and Pt) exhibit 5−10 nm particle sizes, while oxides (PdO and IrO_2) range from 10 to 20 nm. Furthermore, electron dispersive spectroscopy (EDS) mapping images demonstrate homogeneous distribution of Pd and Ir throughout the catalysts without any segregation (Figure S3−4). The combined analysis of XRD, HAADF, and EDS indicates the synthesis of well-defined crystalline catalysts with minimal secondary phases.

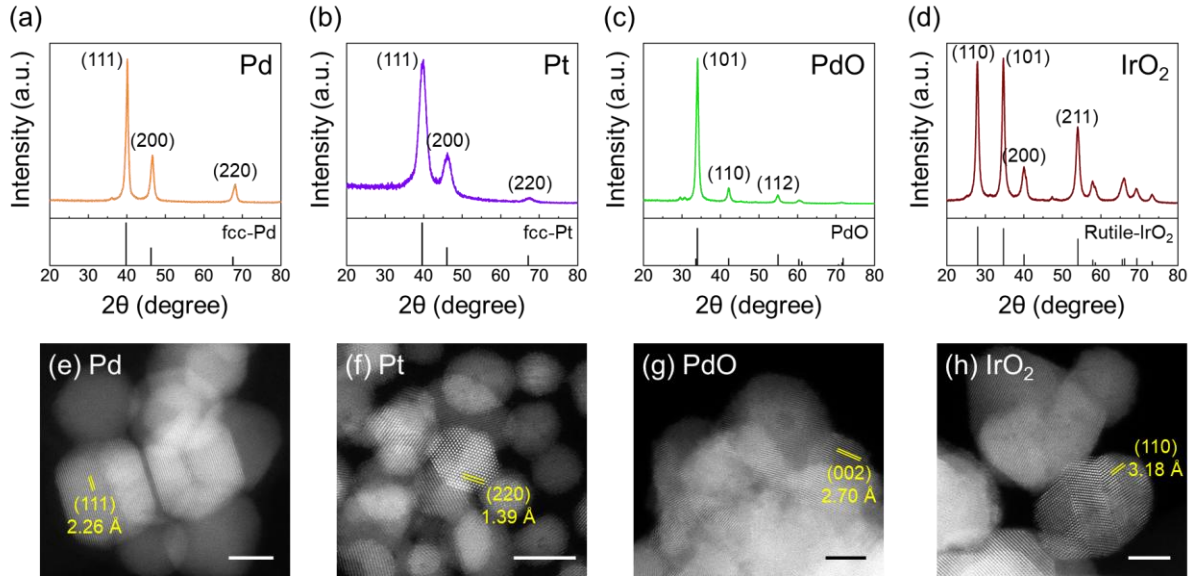

Figure 2. XRD and STEM HAADF images of as-synthesized catalysts. (a)–(d) show the XRD data of Pd, Pt, PdO, and IrO_2, respectively and (e)–(h) the HAADF images. The scale bars in HAADF images represent 5 nm.

The electrochemical oxidation of propylene in aqueous system was first investigated for the different catalysts in a rotating disk electrode (RDE) configuration, in Ar- and propylene-saturated 0.1 M $HClO_4$ (Figure 3 and Figure S5-6). For Pd catalyst (Figure 3a), a single pair of redox peak is observed in the Ar-saturated solution, with a broad oxidation peak visible at 1.1 V *vs.* RHE and a sharp reduction peak at 0.58 V *vs.* RHE corresponding to the formation and reduction of the oxide monolayer on the surface of Pd, respectively.[32–35] In the propylene-saturated solution, a significantly larger oxidative current is detected, likely due to the oxidation of the allyl group in propylene or the desorption of carbon-based adsorbents.[13,18] Pt metal exhibits a similar trend to Pd, with the formation of a PtO surface monolayer at 1.3 V *vs.* RHE,[36,37] and a more pronounced oxidation peak observed in propylene-saturated solution (Figure 3b). By contrast, PdO shows only a small reduction peak at 0.7 V *vs.* RHE in the Ar-saturated solution without any observable oxidation peak, indicating that Pd(II) is not further oxidized (Figure 3c). In propylene-saturated solution, the anodic current is again found to increase at high potentials. For IrO_2, several redox waves are detected in the CV, and are found independent on the presence of propylene (Figure 3d). The oxidation peaks at 1.19 V *vs.* RHE and 1.4 V *vs.* RHE may correspond to the formation of *OH ($H_2O \rightarrow *OH + H^+ + e^-$) and *O ($*OH \rightarrow *O + H^+ + e^-$) adsorbates, respectively, as previously discussed.[38–40] The oxidation peak at 1.4 V *vs.* RHE is difficult to discern due to the onset of the OER, but its position can be inferred from the cathodic peak at 1.35 V *vs.* RHE. In summary, an oxide monolayer is found to form on the surface of Pd and Pt metals at 0.9−1.35 V vs. RHE, oxygenated adsorbates are likely formed on the surface of IrO_2, while no electrochemical sign of surface oxidation was observed for PdO.

Figure 3e−f illustrate the CV collected for these catalysts within the OER range. In Ar-saturated solutions, IrO_2 demonstrates the highest OER activity, followed by Pd metal, PdO, and Pt metal. However, in propylene-saturated solutions, the trend changes significantly. Pd metal and PdO

exhibit little to no difference in propylene-saturated solutions, with only a slight increase in oxidative current recorded (Figure 3e). In contrast, there is a notable decrease in anodic current for IrO_2 and Pt metal (Figure 3f). We hypothesize that the adsorption of propylene hinders water access to the active sites due to the stronger carbon binding energy on the surfaces of Pt metal and IrO_2, thus decreasing the OER activity.[41] Furthermore, clear evidence for the oxidation of PdO at OER potentials is observed after 2 hours of chronoamperometry (CA) at 1.6 V vs. RHE in propylene-saturated 0.1 M $HClO_4$ (Figure S7), with a reduction peak recorded at around 1.3 V *vs.* RHE during backward LSV scan. This observation indicates that further oxidation of Pd (II) into Pd (IV) occurs near 1.6 V *vs.* RHE.

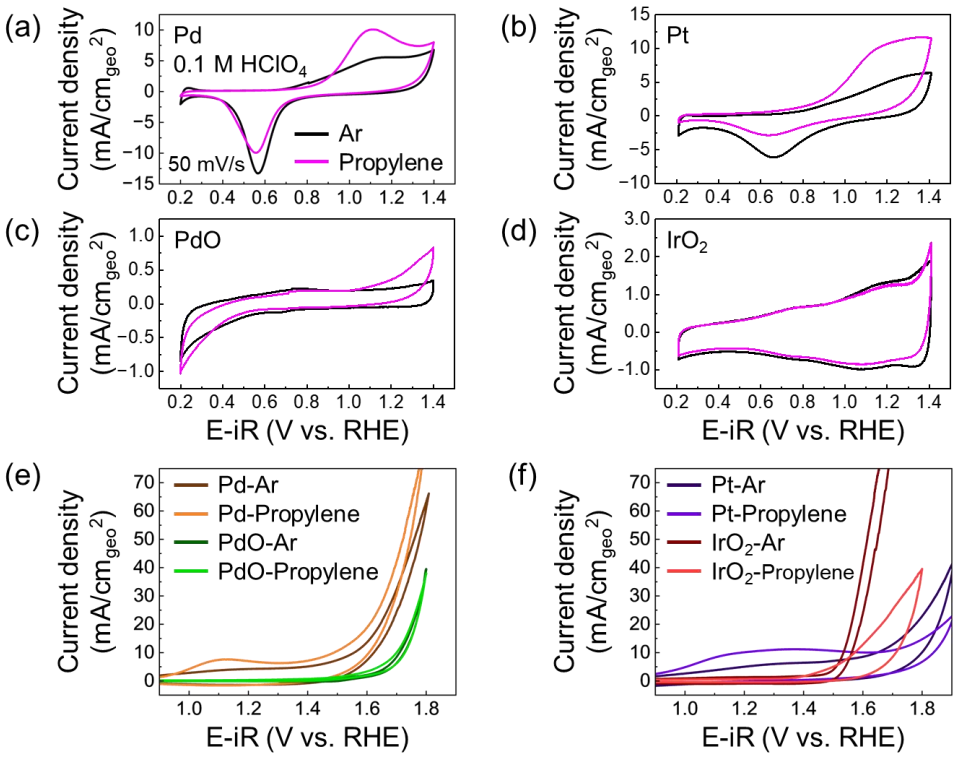

Figure 3. CV curves collected in Ar- and propylene-saturated 0.1 M $HClO_4$ solutions in a potential range between 0.2–1.4 V (vs. RHE) for (a) Pd, (b) Pt, (c) PdO, and (d) IrO_2. CV curves collected at greater anodic potentials (0.2–1.8 V vs. RHE) are presented on (e-f). All the CV curves are collected with a scan rate of 50 mV/s.

Electrocatalysis of Propylene. Electrolysis experiments were then carried out using RDE electrodes under CA conditions, before quantification of the products by ^{1}H-NMR spectroscopy (Figure S8). For Pd, PG is produced post-formation of the oxide layer on the surface (Figure 4a), i.e. at potentials greater than 1.1 V *vs.* RHE (Figure 3a and Figure S9a), corroborating previous studies.[13,15,18] The maximum FE (~23%) for PG formation is observed between 1.35 and 1.40 V *vs.* RHE. At potentials greater than 1.4 V *vs.* RHE, even though the partial current density associated with PG formation increases exponentially, the FE declines due to the overwhelming influence of the OER (Figure S11). A similar trend is noted for the Pt surface (Figure 4b and Figure S9b) for which the highest FE for PG formation is measured at 1.6 V *vs.* RHE; after that, oxide monolayer is formed and the OER becomes predominant. Furthermore, while Pt achieves a slightly higher FE (~27%) than Pd, the partial current density for PG formation is found significantly decreased compared to Pd. Besides PG, acetone was detected at low potentials likely following the homogeneous chemical reaction of propylene with dissolved metal ions, as previously reported $CH_2CHCH_3 + Me^{2+} + H_2O \rightarrow CH_3COCH_3 + Me + 2H^+$.[13,15] Additionally, the C–C cleavage product, acetic acid, was observed, and we anticipate that a certain amount of CO_2 is generated during the reaction. This was accounted for when calculating the FE for different catalysts. However, we did not specifically focus on this product in this study.

For PdO, the onset for the production of PG is observed at 1.45 V *vs.* RHE (Figure 4c), coinciding with the oxidation peak of Pd(II) to Pd(IV) (Figure S9c). The FE peaks at 1.6 V *vs.* RHE, where the OER current starts to dominate. Notably, PdO exhibits a significantly higher FE (55%) than Pd metal. This stark contrast suggests that structural differences between PdO and oxidized Pd surface play a crucial role, as discussed in the next section. Finally, no PG was detected below 1.5 V vs. RHE for IrO_2 (Figure 4d). Above that potential at which an anodic wave corresponding to the formation of Ir*O was previously observed, PG is formed, albeit

with low FE. Hence, for both PdO and IrO_2, the formation of PG is found concomitant with surface oxidation. This finding may indicate that oxo species forming on the surface of metal oxides are crucial intermediates for the formation of PG, while also serving as an intermediate for the OER, as previously discussed.[39,42,43] As a result, propylene oxidation would compete with the OER by sharing the same intermediates, with the OER requiring greater overpotential as a result of slow kinetics associated with steps including deprotonation and O−O bond formation.[39,42,44,45] For all these catalysts, the formation of acetone stops once the surface is oxidized, suggesting that the surface oxide layer or oxo groups passivate the surface and inhibit the dissolution of the catalysts.

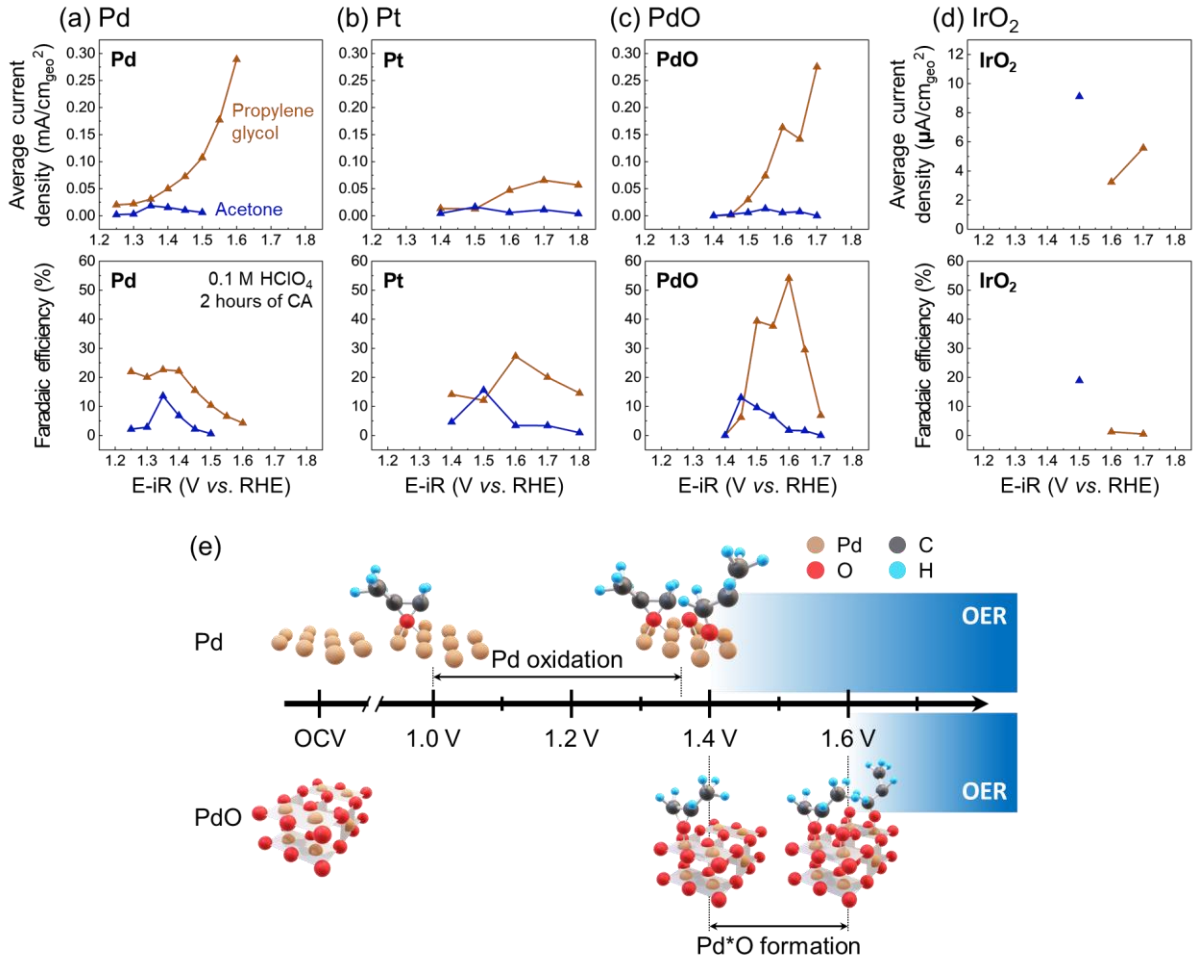

Figure 4. Electrochemical oxidation of propylene in 0.1 M $HClO_4$. The average partial current density and Faradaic efficiency on (a) Pd, (b) Pt, (c) PdO and (d) IrO_2 during 2 hours of CA test are shown. (e) is a schematic figure showing difference in propylene oxidation between Pd and PdO.

Structural effect. Structural differences between Pd and PdO were studied after oxidation using STEM, XAS and X-ray photoelectron spectroscopy (XPS). Figure 5a–b show STEM HAADF images of Pd and PdO surfaces after two hours of CA at 1.40 V *vs.* RHE and 1.60 V *vs.* RHE, respectively. For Pd, the surface remains very clear and crystalline after oxidation (Figure 5a and Figure S13, as confirmed by EDS mapping after CA (Figure S12). Additionally, the extended X-ray absorption fine structure spectroscopy (EXAFS) data shown in Figure 5d

indicate that Pd does not undergo any crystallographic changes upon electrolysis. In contrast, the X-ray absorption near edge spectroscopy (XANES) data shown in Figure 5c and XPS spectra shown in Figure S14 indicates a slight increase in Pd oxidation state, suggesting the formation of surface oxide layer under anodic conditions. However, the structure of this oxide layer remains unclear. Previous studies suggest the formation of an α-PdO monolayer on the surface, which has a lattice structure distinct from bulk PdO. On the other hand, for PdO, the HAADF images in Figure 5b and Figure S15b show that an approximately 1 nm thick amorphous layer forms on the surface, concomitant with the slight increase in oxidation state observed in the XANES and XPS data (Figure 5c and Figure S14). The EXAFS spectra shown in Figure 5e remain largely unchanged, with only a slight decrease in intensity after the CA experiment. Although PdO loses its crystallinity during the CA test and an amorphous layer occurs on the surface, the FE remains high during prolonged experiments (Figure S16). This suggests that the local structure of the amorphous layer closely resembles that of bulk PdO.

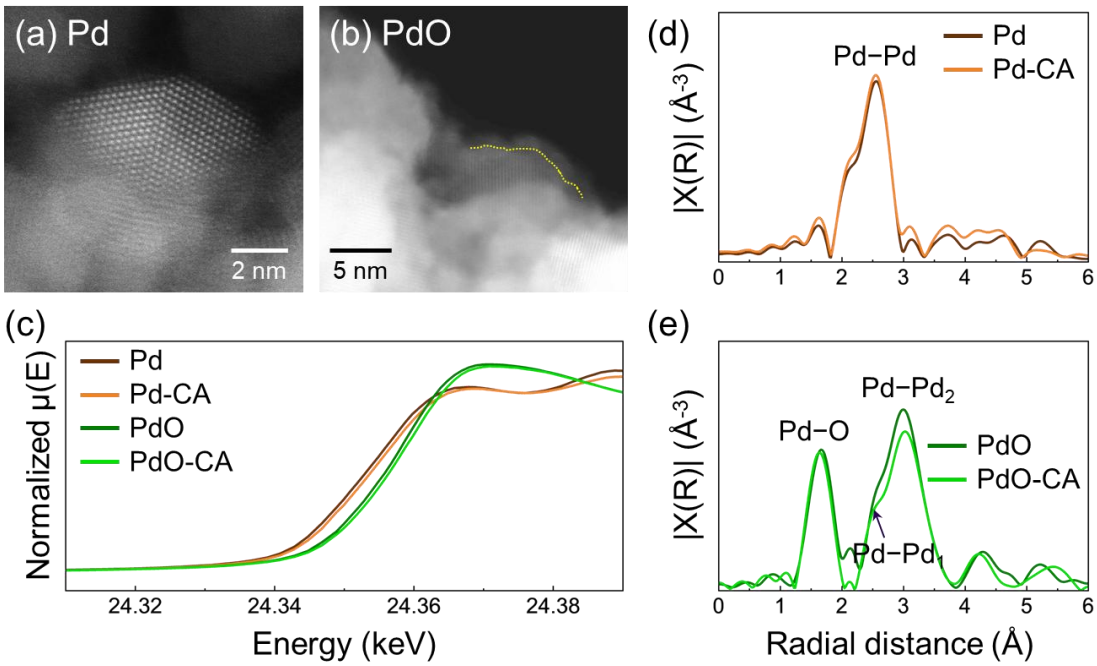

Figure 5. Structural effect in propylene oxidation. STEM HAADF image of (a) Pd and (b) PdO after 2 hours of CA at 1.4 V and 1.6 V in propylene-saturated 0.1 M $HClO_4$, respectively. XANES spectra of both catalysts before and after CA are plotted on (c) and EXAFS data on (d) and (e). The crystal structure of PdO is presented Figure S17.

Pt substitution effect. Previous studies have demonstrated that substitution of Pd-based catalysts can significantly enhance the efficiency of propylene oxidation to PO in near-neutral solutions; this is specifically the case for Pt substitution in PdO.[11] To investigate the effect of Pt substitution under strongly acid conditions, we substituted 25% of Pd atoms by Pt and synthesized Pt25%-PdO. The XRD pattern collected for Pt25%-PdO resembles that of PdO (Figure S18), with a slight shift to lower angles due to the larger ionic radius of Pt compared to Pd. The homogeneity of the sample was further confirmed by EDS, with no secondary phases or segregation observed. Comparing the CV curves to those of Pd and Pt metal in Figure 3a–b, the redox features in the CV curves appear similar to those previously observed for Pt (Figure S19). Additionally, a cathodic feature corresponding to the desorption of oxo adsorbates, alike

previously detected on the surface of PdO, is observed at 1.4 V *vs.* RHE (Figure S19c).

CA experiments were then conducted. At 1.6 V *vs.* RHE, a 67% FE towards PG is obtained, 12% greater than previously measured for PdO (Figure 6a). Compared to previous studies, significantly higher FE are achieved in this work in 0.1 M $HClO_4$ (FE around 25% were previously reported).[12,13] Furthermore, a significantly higher average current density, normalized by the geometric area of the glassy carbon electrode, of 1.82 mA/cm_{geo}^2 at 1.6 V *vs.* RHE was measured compared to PdO (0.16 mA/cm_{geo}^2). Subsequently, the surface areas of PdO and Pt25%-PdO were measured following two methods: the Brunauer, Emmett and Teller (BET) area for gas adsorption and the electrochemically active surface area (ECSA). While BET surface area shows very similar values of 6.3077 m^2/g and 7.0159 m^2/g, respectively, they are contradicted by the ECSA values that show a surface 8 times greater for Pt25%-PdO (Figure S20−21). In light of previous discussion regarding the accuracy and limitations of ECSA analysis,[46] values were normalized by the BET surface area. Using this approach, although Pt substitution only marginally increase the FE of PdO, we find that it likely enhances the current density in the acidic media and thus the intrinsic turnover frequency per active site.

To detect any morphological or structural changes occurring under anodic conditions, STEM HAADF and annular bright field (ABF) images were taken for Pt25%-PdO after the CA at 1.60 V *vs.* RHE (Figure 6b and Figure S22). Pt25%-PdO catalyst shows a clear and crystalline surface after 2 hours of CA (Figure 6b). To understand changes in local geometry and oxidation state, XANES, EXAFS and XPS were collected before and after 2 hours of CA at 1.6 V *vs.* RHE (Figure 6c−d and Figure S23−24). The XANES and EXAFS are found to remain largely unchanged (Figure 6c−d), indicating that the bulk oxidation states and lattice structure are unaltered. However, a slight shift in the XPS spectrum to higher binding energy suggests a minor increase in the oxidation states at the surface (Figure S24). One important feature to note

is the splitting of the metal-metal peak, indicating two characteristic distances when substituting Pd by Pt (See crystal structure in Figure S17). Nevertheless, as discuss above, this does not dramatically impact the electrochemical performance of the catalyst, which shows similar current density and only slightly better FE. However, after 8 hours of CA, an amorphous layer of less than 1 nm of is observed by STEM (Figure S22b), indicating that degradation occurs during prolonged tests.

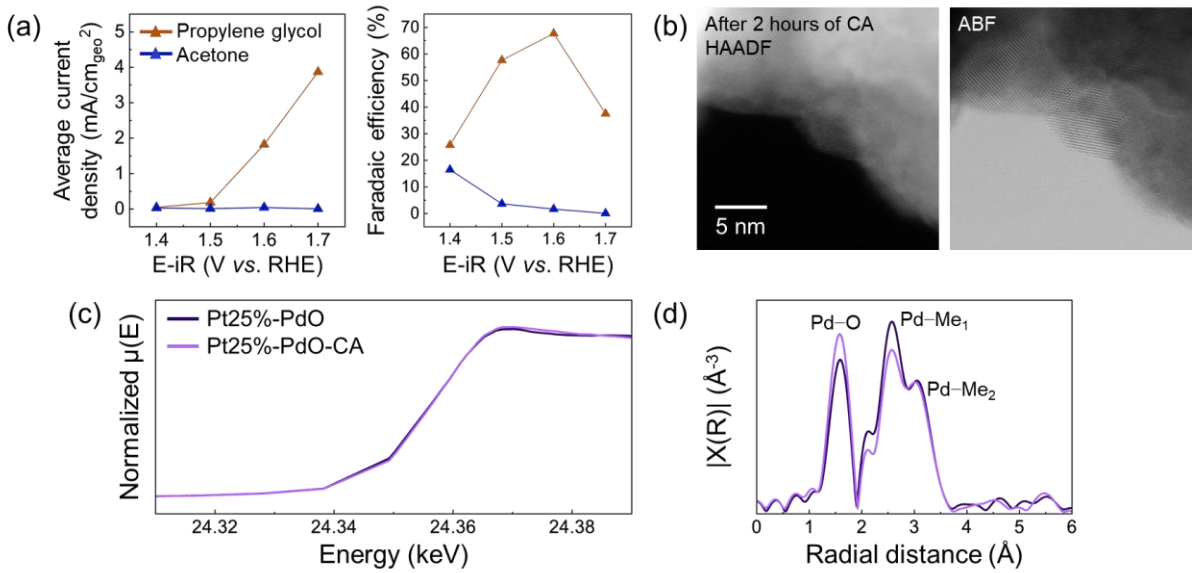

Figure 6. Propylene oxidation on Pt25%-PdO. 2 hours of CA test were conducted in propylene-saturated 0.1 M $HClO_4$. Average partial current density and FE for PG and acetone are shown in (a). HAADF and ABF image of Pt25%-PdO after 2 hours of CA at 1.6 V vs. RHE are presented on (b). XANES and EXAFS spectra collected before and after CA are plotted in (c) and (d), respectively.

To probe reaction intermediates, operando-ATR-FTIR spectroscopy of the electrode/electrolyte interfaces was carried out. The change in absorbance for Pd, PdO and Pd25%-PdO catalysts deposited onto Au electrodes is measured with respect to the initial state of the electrode recorded at an applied potential of 0.8 V *vs.* RHE, during anodic polarization by steps of 0.1 V

followed by cathodic polarization (Figure S25). Figure 7a and Figure S26a shows the potential-dependent spectra recorded for PdO in propylene-saturated 0.1 M $HClO_4$. With increasing electrode potential, several bands develop. However, most of the peaks are largely unchanged upon reversal of the stepping direction, indicating that they are likely arising from irreversible changes of the electrode surface onto products and/or reactants accumulate (Please see Figure S26 for details). [12]

The band at 800 cm^{-1} is only found in propylene-saturated electrolyte, where it shows reversibility with potential, albeit with hysteresis. Such hysteresis is not unexpected, given the complexity of the catalytic interface and the potential-induced changes noted above. Irrespective, this observation establishes the clear potential-dependence of this band, suggestive of a species that is not bound too strongly nor too weakly to the surface, a key condition for a reaction intermediate. This FTIR signal can originate from either a metal-oxo group, which typically appears near 800 cm^{-1}, or a PO- or PG-related peak as the C-C bending of PG[47–49] and the symmetric stretching of the epoxide ring[50,51] in PO also appear near 800 cm^{-1} (Figure S27). To further probe the origin of this peak, one must first observe that this intermediate does not show in Ar-purged 0.1 M $HClO_4$ (Figure 7b), conditions in which only the OER occurs under anodic conditions. Therefore, this intermediate does not originate from an oxo group shared with the OER. Subsequently, a series of spectra were collected using D_2O- and $H_2{}^{18}O$-containing electrolytes saturated with propylene (Figure 7c–e). In D_2O (Figure 7e), the band is found to be invariant, revealing that the intermediate is not protonated. Instead, it is shifted to 760 cm^{-1} in $H_2{}^{18}O$ electrolyte (Figure 7c–d), indicating an oxygenated intermediate that is only observed in propylene-saturated electrolyte. We therefore ascribe this vibration to the symmetric stretching of the epoxide ring in PO. During the first cycle in $H_2{}^{18}O$ electrolyte (Figure 7c), the band at 800 cm^{-1} is observed simultaneously with the band at 760 cm^{-1}, the former disappearing during the second cycle (Figure 7d). This finding suggests that the peak at

800 cm^{-1} originates from oxygen terminal groups initially present on the surface of PdO and that are consumed by reacting with propylene. Furthermore, the peak at 800 cm^{-1} appears around 1.4 V vs. RHE, a potential that coincides with the onset of the anodic current observed for PdO, suggesting that propylene oxidation proceeds sequentially, starting with the formation of an oxo group, followed by the reaction of propylene with this group. Another interesting feature noticed during the second cycle collected in $H_2{}^{18}O$ is the shift of the band at ~840 cm^{-1} to ~815 cm^{-1}. Noting that this peak does not follow the applied potential but instead keeps growing, and based on the peak position and the fact that the associated species contain oxygen, we conclude that it arises from the propylene oxide epoxide ring that accumulate near the electrode upon its production.

By comparing these results with those obtained for Pd metal, for which the band at 800 cm^{-1} is not observed, we conclude that this intermediate only forms on square planar coordination, which is not observed for oxidized Pd surface (Figure S28). Finally, to comprehend the effect of Pt substitution on PdO, similar measurements were collected with Pt25%-PdO (Figure 7f and Figure S26f). Once again, the peak at 800 cm^{-1} is detected, indicating that Pt substitution does not modify the active site for propylene oxidation and that similar oxygenated intermediate is formed. Following previous works,[17] we propose that PG formation on PdO and Pt25%-PdO follows the Eley-Rideal mechanism in which the vinyl group of propylene interacts with the oxide and oxo adsorbates, forming a C−O−C triangular ring that subsequently desorbs as PO before to be hydrolyzed in acidic conditions into PG. Our results suggest that adsorbates responsible for propylene oxidation preferentially forms for Pd in square planar coordination, for which undercoordinated apical sites are directly accessible (Figure 7g). Instead, the oxide monolayer forming on the surface of Pd, for which the Pd-Pd bond distance is much shorter than that in PdO (as observed in the EXAFS spectra Figure 5d−e), shows different behavior compared to the PdO.

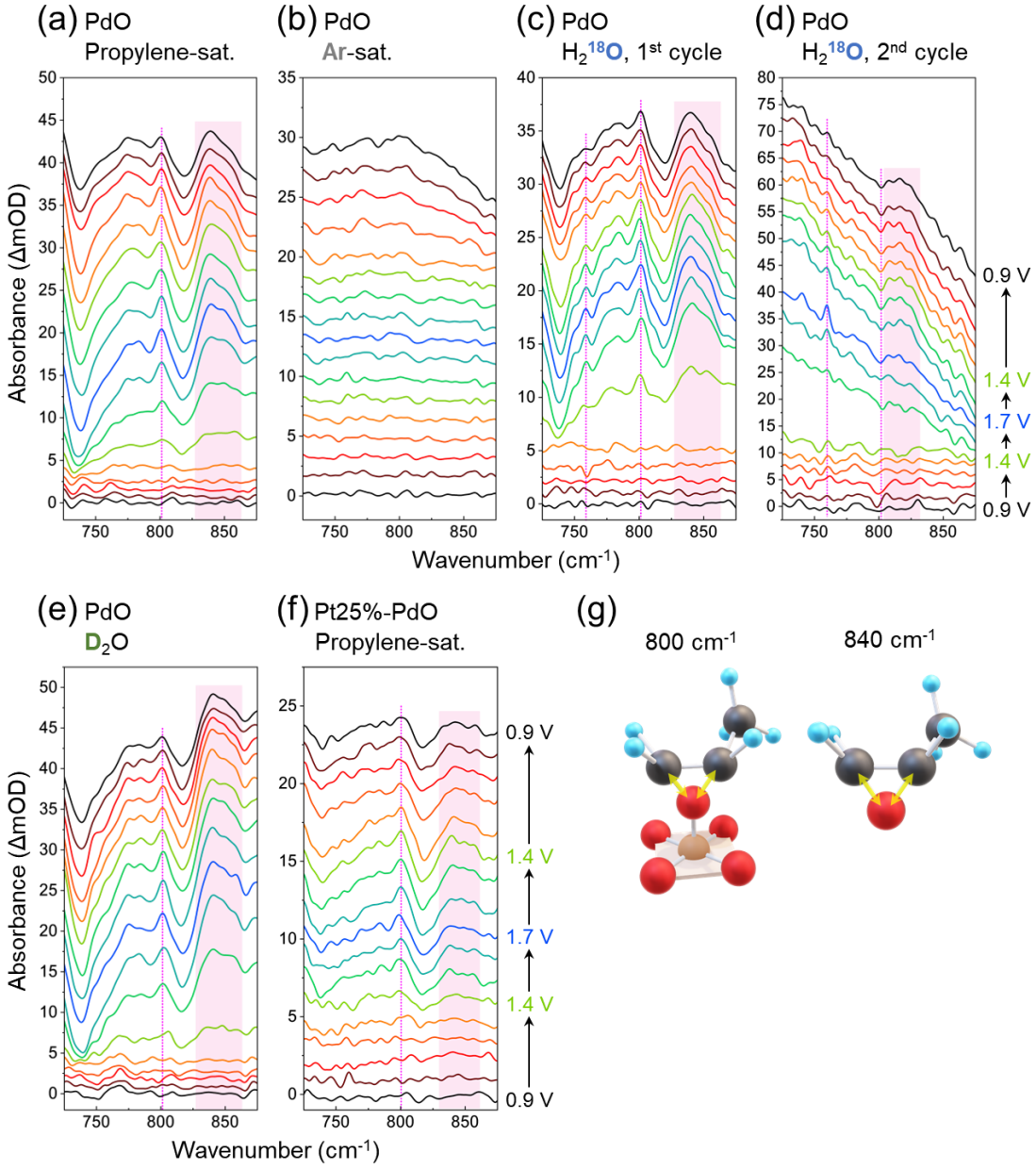

Figure 7. *Operando* FTIR spectra. FTIR spectra of PdO were collected under varying applied potentials in (a) a propylene-saturated solution and (b) an Ar-saturated solution. Isotope labeling tests were performed using (c) $H_2{}^{18}O$-1st cycle, (d) $H_2{}^{18}O$-2nd cycle and (e) deuterated solution are shown. Additionally, FTIR spectra of (f) Pt25%-PdO in a propylene-saturated solution were obtained. (g) Schematic illustration of the intermediate and product are shown.

Propylene oxidation in different environments. Having established the design principles

controlling the selectivity and kinetics for propylene oxidation into PG in acidic conditions, namely the presence of square planar local coordination onto which oxo intermediates reacting with propylene are formed, our attention then turned to understanding if similar design principles would apply in near-neutral environment. The electrochemical results obtained using an RDE setup and the Pt25%-PdO catalyst in propylene-saturated phosphate buffer solutions (PBS, 0.25 M sodium phosphate + 0.9 M sodium perchlorate) are shown in Figure S29. First, a broad reduction peak is observed in CV scan at 1.0−1.4 V *vs.* RHE (red arrow), indicative of an oxidation event occurring at potentials greater than 1.4 V *vs.* RHE. Alike the results previously obtained in acid, the FE for PO formation is found to increase after the anodic activation of the surface (1.7 V *vs.* RHE). The maximum FE toward PO obtained under these conditions was of 13% at 1.9 V *vs.* RHE, much lower than the FE towards the production of PG previously measured in acid and much lower compared to previous report of FE: 51% and 60% in PBS and aqueous-organic hybrid electrolytes, respectively.[11] To decipher the origin for this large difference in FE as function of the electrolyte, PO was dissolved in the PBS solution, and conditions similar to the RDE experiments were applied: the glassy carbon electrode was rotated at 1600 rpm and propylene gas was purged over the headspace for 2 hours. The ^{1}H-NMR spectra collected after the experiment show that very little PO remains (Figure S30). This observation indicates that the high volatility of PO, which has a low boiling point of 30°C, induces its rapid evaporation after formation.

To achieve high-efficiency PO production, electrolysis experiments were carried out using a gas-diffusion electrode (GDE) in place of the RDE setup. The electrodes were designed to resemble conditions previously reported in flow cells[11,19,20] (Figure S31 and see Methods section for a full description). In brief, one compartment of an H-cell was filled with electrolyte and completely sealed to avoid PO evaporation. The other compartment served as a gas reservoir in which propylene was constantly flowing. The working electrode was positioned at

the center of the H-cell, and a substantial amount of Nafion was applied, facilitating gas diffusion to the electrode surface while creating a hydrophobic interface to slow down the OER. Figure 8a shows the FE obtained for propylene oxidation in 0.1 M $HClO_4$ and in PBS using Pt25%-PdO. A significant increase in FE was observed in both solutions when compared to the results gathered in RDE conditions. In PBS, *i.e.* in near-neutral conditions, a 51% FE towards PO was achieved at 2.0 V *vs.* RHE, consistent with previous reports.[11] In 0.1 M $HClO_4$ (pH 1), a 100% FE towards PG was achieved at 1.7 V *vs.* RHE. The large FE difference between the RDE and GDE experiments is attributed to the cell design. Indeed, in the RDE setup, limited amount of Nafion is used and both propylene and water have a relatively good access to the catalyst surface (Figure 8b). However, the reaction is limited by the low concentration of propylene dissolving in the aqueous solutions, in the order of 5.6 mM at 25°C.[52] In contrast, the use of GDE allows propylene to flow through the porous carbon electrode and reach the Pd-based catalysts on the side opposite to the aqueous electrolyte.[53] Additionally, the substantial amount of hydrophobic Nafion applied to the electrode surface restricts excessive water access, thereby largely suppressing the OER (See supplementary note 1). Therefore, by increasing propylene activity and decreasing water activity, a higher oxidative potential (1.7 V *vs.* RHE) can be applied in H-cell, leading to a larger production rate and an enhanced propylene oxidation efficiency across both pH conditions. In short, our experiments show that extrinsic factors are as, if not more, important when compared to intrinsic activity towards propylene oxidation to achieve large FE towards the production of PG or PO.

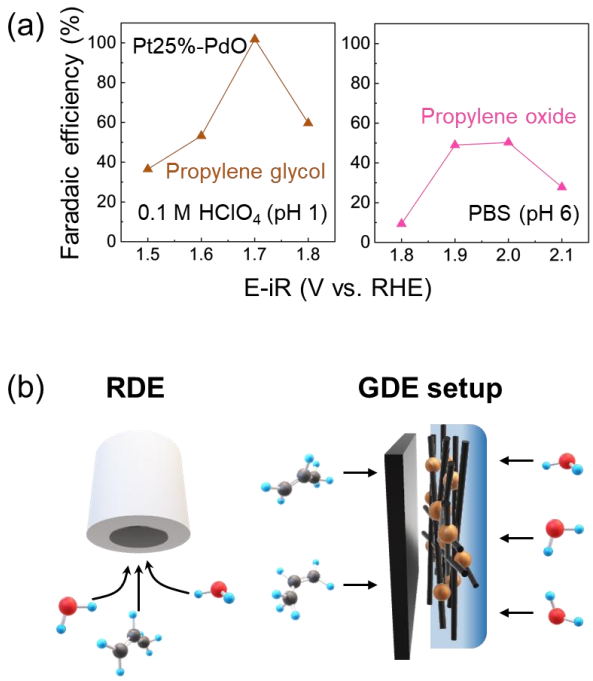

Figure 8. Propylene oxidation recorded using a gas-diffusion electrode (GDE) configuration. CA experiments were conducted in 0.1 M $HClO_4$ and PBS using GDE setup. FE for PG and PO are plotted in (a). Schematic figures showing difference between RDE and GDE configurations are shown in (b).

Having demonstrated that the experimental setup significantly impacts the reaction outcome, we next investigated the effect of pH on propylene oxidation. Propylene oxidation experiments were conducted in the RDE setup under varying pH conditions. When comparing the results on the RHE scale (Figure S32a), the Faradaic efficiency and the onset potential of the partial current density for propylene-related products (PO and PG) shift significantly toward higher anodic potentials as pH increases, whereas the onset potential of the total current density remains largely unchanged. Instead, when plotted against the SHE scale, the maximum FE occurs at similar potentials across different pH conditions (Figure 9a). Additionally, the onset potential of the average partial current density is found independent on pH (Figure 9c). This observation suggests the existence of a potential-determining step[54] for the propylene oxidation

into PO and PG, for which proton is not involved, resulting in a pH-independent onset potential for propylene oxidation to PO and PG. In contrast to the propylene oxidation, the average total current density is shifted towards cathodic potential with increasing pH in the RDE configuration (Figure 9b), owing to the OER current which becomes predominant as thermodynamically shifted to cathodic potential with pH (Figure S34).

By combining the electrochemical results with ATR-FTIR data, a new mechanistic model for propylene oxidation on Pd-based oxides is proposed (Figure 9d). Similar to the conventional OER mechanism, ① hydroxyl groups first adsorb onto the PdO surface, followed by ② an uncoupled proton-electron transfer step, leaving behind a negatively charged oxo species. Subsequently, ③ propylene interacts with this oxo species, forming complex intermediates detected via operando ATR-FTIR. Based on electrochemical results, the standard reduction potential for this step is estimated to be approximately 1.3 V (vs. SHE). ④ Desorption of this intermediate is likely facilitated by a chemical reaction, which explains the partial reversibility of the peak at 800 cm^{-1} with varying potential. Furthermore, our work indicates that the propylene oxidation mechanism and the potential determining intermediates are similar in acidic and near-neutral conditions; in other words, it suggests that PG is likely produced by the hydrolysis of PO in acidic conditions, not by a direct electrochemical oxidation mechanism, in agreement with previous conclusions.[10,17] On the other hand, the onset potential of the total current density shifts anodically by ~0.059 V per pH, indicating that a proton-coupled electron transfer step is the rate-determining step for the OER, likely the *OOH formation as previously observed.[39,42]

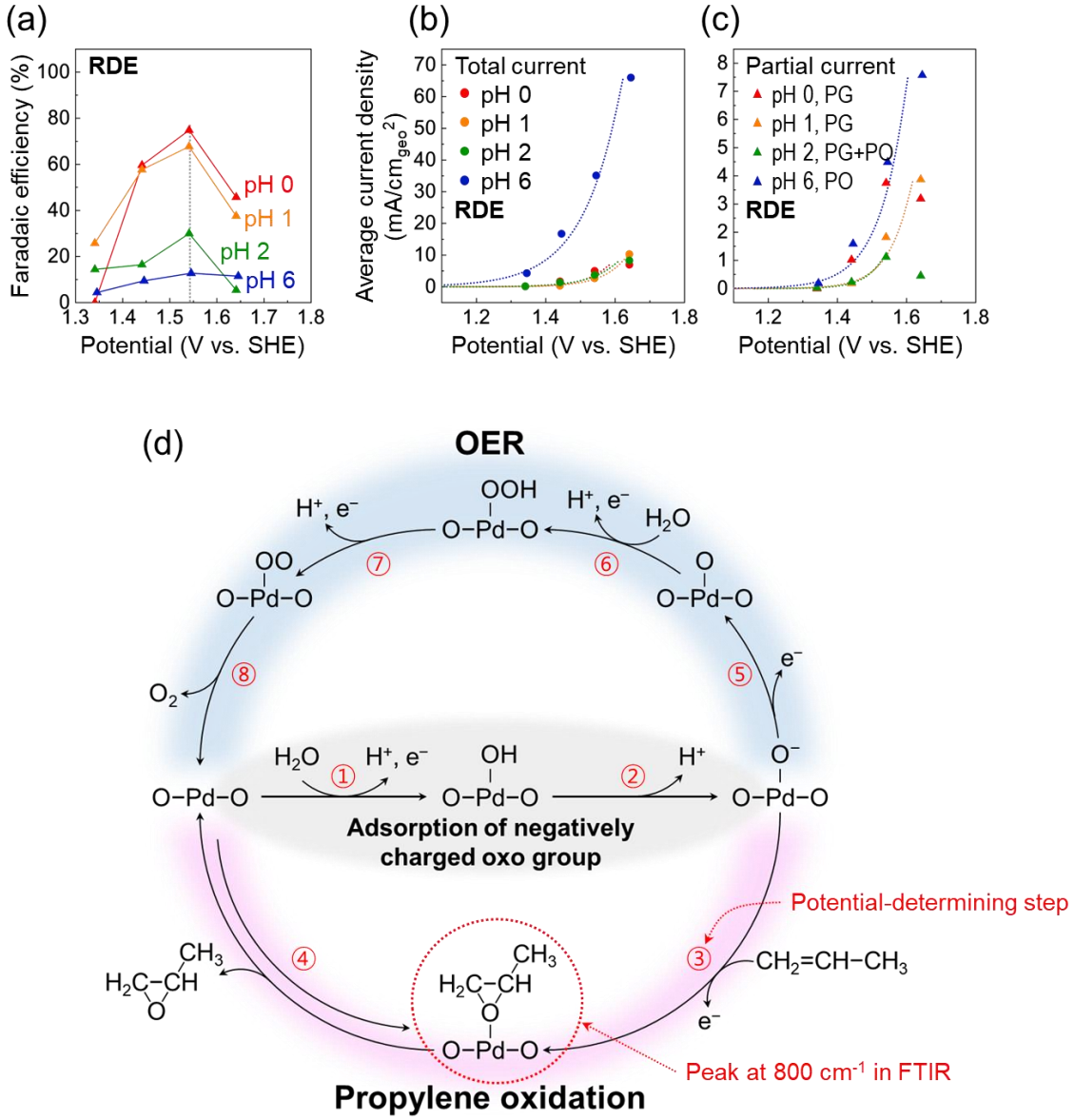

Figure 9. Propylene oxidation in various pH and propylene oxidation mechanism. (a) Faradaic efficiency, (b) average total current density and (c) partial current density in various pH conditions are plotted on the SHE scale. Schematic illustration of the propylene oxidation mechanism are shown on (d). 1 M $HClO_4$ and 0.01 M $HClO_4$ + 0.2 M $NaClO_4$ solutions are used for the pH 0 and pH 2 electrolytes, respectively.

Conclusion

In this study, we demonstrate that both intrinsic catalytic properties and extrinsic properties explain the large FE observed for Pd-based catalysts towards PG and PO formation. Operando ATR-FTIR experiments using isotopic labelling reveal the formation of surface oxo intermediates forming on unsaturated PdO surface, while no such intermediate is observed for oxidized Pd surface. These intermediates result from the reaction of surface oxo species with propylene and differ from oxo intermediates involved into the OER. Furthermore, we demonstrate that similar intermediates are formed on the surface of Pt-substituted PdO, indicating that Pt substitution does not modify the active sites. Careful electrocatalytic study further shows that Pt substitution does not alter the FE significantly, but likely enhances the intrinsic activity of the catalyst in acidic media. Our work further highlights that the outcome of this reaction largely depends on extrinsic factors independent on the catalyst but dependent on the design of the electrochemical cell. Indeed, GDE used in H-cell setup prevents PO evaporation while reducing water activity and increasing the accessibility of propylene in the gas phase, all leading to a significant increase in FE found for Pt25%-PdO catalyst in both 0.1 M $HClO_4$ and PBS. Especially, 100% FE towards PG was achieved on Pt25%-PdO using GDE in the H-cell configuration. Finally, by comparing the results obtained in acidic and near neutral conditions, we demonstrate that the onset potential for propylene oxidation is pH independent and that the reaction involves non-protonated oxo intermediates, as detected by operando ATR-FTIR. This observation confirms that PG is formed in acidic conditions by the hydrolysis of PO. Furthermore, it indicates the existence of a potential determining step for propylene oxidation, which forms at around 1.3 V *vs.* SHE. Overall, our work highlights that both a careful design of selective Pd-based catalysts coupled with a proper mastery of interfacial properties including hydrophilicity and gas permeation properties are necessary to achieve sufficient current densities and FE for propylene oxidation in aqueous electrolytes to be considered as a viable synthetic alternative to more established routes.

Methods

Synthesis of catalysts. All catalysts in this study were synthesized using the polyol method[29–31] with $PdCl_2$ (99.9%, Sigma Aldrich), $H_2PtCl_6 \cdot 6H_2O$ (37.5% Pt basis, Sigma Aldrich), and $IrCl_3 \cdot xH_2O$ (reagent grade, Sigma Aldrich) serving as metal precursors. A 1 mmol quantity of the metal precursors was mixed in 120 mL of ethylene glycol (99.8%, Sigma Aldrich). To this solution, 1 g of polyvinylpyrrolidone (PVP, Mw: 10,000, Sigma Aldrich) was added as a capping agent under vigorous stirring. The solution was then refluxed at 160°C for 3 hours, with Ar purging for metal synthesis and without purging for metal oxide synthesis. After the reaction, the solution was cooled to room temperature and mixed with acetone in a 1:3 ratio, and the resulting particles were separated by centrifugation at 7500 rpm for 10 minutes. The particles were then washed again with a 1:3 ethanol and acetone mixture. The centrifuged particles were collected in a crystallizing dish using acetone and dried in a vacuum oven at 80°C overnight. For the metal oxides, an additional heat treatment was conducted to oxidize the particles by calcining them at 450°C for PdO, 500°C for Pt25%-PdO, and 550°C for IrO_2, all for 24 hours in an O_2 atmosphere. To determine whether the particles were synthesized properly, phase identification was performed by X-ray diffractometry (D2 Phaser, Bruker) with a Cu $K_{\alpha1}/K_{\alpha2}$ source.

Electrochemical measurements. All electrochemical tests were performed using a VSP potentiostat (Biologic). A 0.1 M $HClO_4$ solution was prepared by mixing Milli-Q water (18.2 MΩ·cm) with 70% $HClO_4$ (99.999%, Sigma-Aldrich). A 0.25 M phosphate buffer solution (pH 6) was prepared by combining Na_2HPO_4 (99%, Oakwood Chemical) and NaH_2PO_4 (UPS grade, Oakwood Chemical) with 0.9 M $NaClO_4$ (98%, Oakwood Chemical) in Milli-Q water. Electrochemical analyses were conducted in a three-electrode system using a leakless Ag/AgCl

electrode as the reference and a Pt wire as the counter electrode, with the counter electrode separated by a glass frit to prevent the reduction of substrates and products. Uncompensated resistance was measured by electrochemical impedance spectroscopy before each experiment, and all experiments were conducted with 85% ohmic drop correction in the EC-Lab software. The measured potentials were converted to the RHE scale using the following equations:

$$E_{RHE} = E_{measured} + 0.059 \cdot pH + E^{\circ}_{ref}$$

Rotating disk electrode. We conducted the electrochemical tests with rotating disk electrodes using a rotator (AFMSRCE, PINE research) at 1600 rpm. 13.1 mg of catalysts were mixed in ethanol with acetylene black and 5-wt% Nafion dispersion (Nafion^{TM} D520CS, Ion Power). The total volume of the ink was 2 mL with a 10:1:1 mass ratio between catalysts, acetylene black, and Nafion. After sufficient vortexing of the ink, it was sonicated for 1 h and drop-casted onto a glassy carbon disk electrode (5 mm in diameter, PINE research) such that the amount of catalysts loaded on the disk electrode was 0.4 mg/cm^2. The electrode was then dried at 60°C in a drying oven for 2h. Before the electrochemistry, the gas was bubbled directly inside the electrolyte and purged at the headspace during the test.

Gas diffusion setup. For the H-cell experiment, hydrophobic carbon paper (Toray Carbon Paper 120, 5% wet-proofed, FuelCell Store) was punched into 19 mm-diameter disks and annealed in a box furnace at 600°C for 1 hour in air to increase surface energy and remove surface coatings that could affect electrocatalysis. The ink for the H-cell experiment was prepared by mixing the catalyst in a water-ethanol solution (3:1 volumetric ratio) and sonicated for 1 hour. The final ink contained 4 mg/mL of the catalyst without the addition of acetylene black or Nafion. A volume of 92.1 μL of the ink was drop-cast onto the baked carbon paper and dried at 80°C in a vacuum oven. This procedure was repeated three more times, resulting in a total of 368.4 μL of ink being applied to the electrode. Following this, 92.1 μL of a 2-wt% Nafion

dispersion (prepared by diluting 5-wt% Nafion with water) was drop-cast onto the electrode and then dried in a vacuum oven at 80°C for 2 hours.

Figure S31 shows the electrochemical cell setup of the H-cell. One part of the H-cell was entirely filled with the electrolyte without any headspace and perfectly sealed to impede the evaporation of PO. The opposite compartment was purged with propylene gas before the electrochemical reaction, and a slow flow of propylene gas was maintained during the experiment. The working electrode was positioned centrally between the two chambers, with 6 mm of the prepared electrode directly exposed to the electrolyte. Hydrophobic carbon paper was placed at the back of the electrode to prevent electrolyte leakage and allow gas penetration to the working electrode. A Leakless Ag/AgCl electrode was used as the reference, and Pt was used as a counter electrode in the isolation chamber to prevent product reduction and pressure build-up.

Product analysis. All products were quantified using ^{1}H-NMR. After the electrochemical reactions, 430 μL of electrolyte was directly transferred into an NMR tube along with 100 μL of 5 mM dimethyl sulfoxide (99.9%, Sigma Aldrich) as an internal standard, and a D_2O insert for lock. The ^{1}H-NMR spectra were obtained using an NMR spectrometer (Advance Neo, Bruker) operating at 500 MHz under water-suppression mode. Locking, shimming, tunning, and gain setting were performed automatically. 64 scans were collected per sample. The data were processed with MestReNova software for phase correction and background removal.

STEM and EDS. For TEM sample preparation, small amounts of synthesized particles were dispersed in ethanol via sonication and dropped on the lacey carbon-supported copper grids (Oxford Instruments). For samples after the CA, catalysts on the RDE were separated using sonication in ethanol and then dropped on the TEM grids. HAADF and ABF STEM images were taken with a transmission microscope (Titan Themis Z G3 Cs-corrected S/TEM, Thermo

Fischer Scientific) at 200 kV with a spherical aberration corrector. Element mapping with EDS was also carried out using Themis Z G3 at 200 kV along with Super X-4 quadrant EDS detector (ChemiSTEM^{TM} technology). Pd Lα (2.8 keV), Pt Lα (9.4 keV) and Ir Lα (9.2 keV) lines were selected during chemical mapping. The probe current was adjusted to be 150 pA with a scanning time of < 300 seconds.

XPS and XAS. For the XAS and XPS analysis, the samples were prepared on carbon paper. The same ink for the RDE experiments were used. 50 μL of ink was dropped on the carbon paper and dried in vacuum oven at 80°C for 2 hours. Post-CA test, samples were rinsed with DI water and dried by air blowing. The valence state of Pd at the surface of the catalysts was investigated by XPS analysis. *Ex-situ* XPS spectra of Pd 3*d* was collected using X-ray photoelectron spectroscope (K-Alpha XPS, ThermoFisher) with monochromatic Al-K_α radiation (1486.7 eV) and flood gun emission of 150 μA. *Ex-situ* XAS spectra of Pd *K*-edge was collected in X-ray fluorescence mode. Measurements were carried out at the 7D beamlines of PLS-II for Pd metal and PdO and at the BAMline of BESSY II (Helmholtz-Zentrum Berlin für Materialien und Energie)[55] for Pt25%-PdO. Fourier transforms were performed between 20 and 550 eV (2.3 to 12.0 $Å^{-1}$) relative to E_0 = 24.35 keV using a Cosine window applied to 0.1% of the data.

ATR-FTIR. *Electrode preparation.* Au thin films were electrolessly deposited onto Si wafers with micromachined grooves (dimensions: 11 mm × 9 mm × 0.5 mm; 35° groove angle, IRUBIS GmbH) according to a reported method.[43] After the deposition of the Au thin films, the ink containing the catalysts (Pd, PdO or Pt25%-PdO, the same ink for the RDE) was cast on the Au films, achieving 0.2 mg/cm^2, and the films were dried in the vacuum oven at 80°C for 2 hours.

ATR-FTIR spectroelectrochemistry settings. The catalyst/electrolyte interface during

electrochemical propylene oxidation was monitored with FTIR spectroscopy in attenuated total reflection (ATR) mode. A Bruker Vertex 70 FTIR spectrometer equipped with a liquid-nitrogen-cooled MCT detector (FTIR-16, Infrared Associates) was used. An infrared longpass filter (cut-on wavelength: 2.4 μm, #68653, Edmund Optics) was installed in front of the detector. The angle of incident infrared radiation was 50°, which is the optimum angle for the used μ-groove ATR wafer. The prepared electrode was assembled into a customized polyether ether ketone spectroelectrochemical cell and coupled with an ATR accessory (VeeMax III, Pike Technologies). A schematic of the cell is shown in a prior publication.[43] Ag/AgCl/NaCl (3 M) electrode (RE-5B, BASi) and a graphite rod (1/8" diameter, Electron Microscopy Sciences) served as reference and counter electrodes, respectively.

Data collection. The catalyst-decorated Au films were first subjected to 2 CVs (0.2−1.4 V *vs*. RHE for Pd-metal and 0.8−1.4 V *vs*. RHE for PdO and Pt25%-PdO) at a scan rate of 50 mV/s in Ar- or propylene-saturated 0.1 M $HClO_4$ for the surface activation. Following this preconditioning, the potential was stepped in 0.1 V increments from 0.8 to 1.6 V *vs*. RHE for Pd and 0.8 to 1.7 V *vs*. RHE for PdO and Pt25%-PdO. After reaching the most positive potential, the potential was stepped back to 0.8 V *vs*. RHE again in 0.1 V increments (Figure S25). Each potential was held for 1 min. Interferograms were recorded in doublesided/forward-backward mode. Single-beam spectra were collected 30 s after the desired potential was applied; each spectrum took ~28 s to collect. The spectral resolution was 4 cm^{-1} and the scanner velocity was 40 kHz. The change in optical density was calculated using $A = -1000 * \log_{10}(S/R)$, where S and R represent the single-beam sample spectrum and single-beam reference spectrum, respectively. The first spectrum collected at 0.8 V *vs*. RHE was used as the reference spectrum.

Acknowledgements

This work was supported by the National Research Foundation of Korea (grant number RS-2024-00413539) and the National Science Foundation Major Research Instrumentation (NSF-MRI) Program (award number CHE-2117246). We acknowledge technical support with 7D beamlines of the Pohang Light Source-II in the Pohang Accelerating Laboratory. We also thank the Helmholtz-Zentrum Berlin für Materialien und Energie for the allocation of synchrotron radiation beamtime. Part of this work was conducted at the MIT. Nano Characterization Facilities.

References

(1) Morales-Guio, C. G.; Cave, E. R.; Nitopi, S. A.; Feaster, J. T.; Wang, L.; Kuhl, K. P.; Jackson, A.; Johnson, N. C.; Abram, D. N.; Hatsukade, T.; Hahn, C.; Jaramillo, T. F. Improved CO_2 Reduction Activity towards C2+ Alcohols on a Tandem Gold on Copper Electrocatalyst. *Nat. Catal.* **2018**, *1* (10), 764–771. https://doi.org/10.1038/s41929-018-0139-9.

(2) Xu, A.; Hung, S. F.; Cao, A.; Wang, Z.; Karmodak, N.; Huang, J. E.; Yan, Y.; Sedighian Rasouli, A.; Ozden, A.; Wu, F. Y.; Lin, Z. Y.; Tsai, H. J.; Lee, T. J.; Li, F.; Luo, M.; Wang, Y.; Wang, X.; Abed, J.; Wang, Z.; Nam, D. H.; Li, Y. C.; Ip, A. H.; Sinton, D.; Dong, C.; Sargent, E. H. Copper/Alkaline Earth Metal Oxide Interfaces for Electrochemical CO_2-to-Alcohol Conversion by Selective Hydrogenation. *Nat. Catal.* **2022**, *5* (12), 1081–1088. https://doi.org/10.1038/s41929-022-00880-6.

(3) Li, K.; Andersen, S. Z.; Statt, M. J.; Saccoccio, M.; Bukas, V. J.; Krempl, K.; Sažinas, R.; Pedersen, J. B.; Shadravan, V.; Zhou, Y.; Chakraborty, D.; Kibsgaard, J.; Vesborg, P. C. K.; Nørskov, J. K.; Chorkendorff, I. Enhancement of Lithium-Mediated Ammonia Synthesis by Addition of Oxygen. *Science* **2021**, *374* (6575), 1593–1597. https://doi.org/10.1126/science.abl4300.

(4) Iriawan, H.; Andersen, S. Z.; Zhang, X.; Comer, B. M.; Barrio, J.; Chen, P.; Medford, A. J.; Stephens, I. E. L.; Chorkendorff, I.; Shao-Horn, Y. Methods for Nitrogen Activation by Reduction and Oxidation. *Nat. Rev. Methods Primers* **2021**, *1* (1), 56. https://doi.org/10.1038/s43586-021-00053-y.

(5) Dorchies, F.; Serva, A.; Crevel, D.; De Freitas, J.; Kostopoulos, N.; Robert, M.; Sel, O.; Salanne, M.; Grimaud, A. Controlling the Hydrophilicity of the Electrochemical Interface to Modulate the Oxygen-Atom Transfer in Electrocatalytic Epoxidation Reactions. *J. Am. Chem. Soc.* **2022**, *144* (49), 22734–22746. https://doi.org/10.1021/jacs.2c10764.

(6) Chung, M.; Jin, K.; Zeng, J. S.; Ton, T. N.; Manthiram, K. Tuning Single-Atom Dopants on Manganese Oxide for Selective Electrocatalytic Cyclooctene Epoxidation. *J. Am. Chem. Soc.* **2022**, *144* (38), 17416–17422. https://doi.org/10.1021/jacs.2c04711.

(7) Lin, X.; Zhou, Z.; Li, Q.; Xu, D.; Xia, S.; Leng, B.; Zhai, G.; Zhang, S.; Sun, L.; Zhao, G.; Chen, J.; Li, X. Direct Oxygen Transfer from H_2O to Cyclooctene over Electron-Rich RuO_2 Nanocrystals for Epoxidation and Hydrogen Evolution. *Angew. Chem.* **2022**, *134* (35), e202207108. https://doi.org/10.1002/ange.202207108.

(8) Jin, K.; Maalouf, J. H.; Lazouski, N.; Corbin, N.; Yang, D.; Manthiram, K. Epoxidation of Cyclooctene Using Water as the Oxygen Atom Source at Manganese Oxide Electrocatalysts. *J. Am. Chem. Soc.* **2019**, *141* (15), 6413–6418. https://doi.org/10.1021/jacs.9b02345.

(9) Ghosh, R.; Hopping, G. M.; Lu, J. W.; Hollyfield, D. W.; Flaherty, D. W. Alkene Epoxidation and Oxygen Evolution Reactions Compete for Reactive Surface Oxygen Atoms on Gold Anodes. *J. Am. Chem. Soc.* **2025**, *147* (2), 1482–1496. https://doi.org/10.1021/jacs.4c08948.

(10) Yilmaz, T.; Qiao, Y.; Chorkendorff, I.; Seger, B. Direct Electrocatalytic Propylene Epoxidation on PdO_x and PtO_x. *J. Phys. Chem. C* **2024**, *128* (40), 17006–17012. https://doi.org/10.1021/acs.jpcc.4c05592.

(11) Chung, M.; Maalouf, J. H.; Adams, J. S.; Jiang, C.; Román-Leshkov, Y.; Manthiram, K. Direct Propylene Epoxidation via Water Activation over Pd-Pt Electrocatalysts. *Science* **2024**, *383* (6678), 49–55. https://doi.org/10.1126/science.adh4355.

(12) Liu, X. C.; Wang, T.; Zhang, Z. M.; Yang, C. H.; Li, L. Y.; Wu, S.; Xie, S.; Fu, G.; Zhou, Z. Y.; Sun, S. G. Reaction Mechanism and Selectivity Tuning of Propene Oxidation at the Electrochemical Interface. *J. Am. Chem. Soc.* **2022**, *144* (45), 20895–20902. https://doi.org/10.1021/jacs.2c09105.

(13) Winiwarter, A.; Silvioli, L.; Scott, S. B.; Enemark-Rasmussen, K.; Sariç, M.; Trimarco, D. B.; Vesborg, P. C. K.; Moses, P. G.; Stephens, I. E. L.; Seger, B.; Rossmeisl, J.; Chorkendorff, I. Towards an Atomistic Understanding of Electrocatalytic Partial Hydrocarbon Oxidation: Propene on Palladium. *Energy. Environ. Sci.* **2019**, *12* (3), 1055–1067. https://doi.org/10.1039/c8ee03426e.

(14) Ke, J.; Chi, M.; Zhao, J.; Liu, Y.; Wang, R.; Fan, K.; Zhou, Y.; Xi, Z.; Kong, X.; Li, H.; Zeng, J.; Geng, Z. Dynamically Reversible Interconversion of Molecular Catalysts for Efficient Electrooxidation of Propylene into Propylene Glycol. *J. Am. Chem. Soc.* **2023**, *145* (16), 9104–9111. https://doi.org/10.1021/jacs.3c00660.

(15) Huang, J. E.; Chen, Y.; Ou, P.; Ding, X.; Yan, Y.; Dorakhan, R.; Lum, Y.; Li, X. Y.; Bai, Y.; Wu, C.; Fan, M.; Lee, M. G.; Miao, R. K.; Liu, Y.; O'Brien, C.; Zhang, J.; Tian, C.; Liang, Y.; Xu, Y.; Luo, M.; Sinton, D.; Sargent, E. H. Selective Electrified Propylene-to-Propylene Glycol Oxidation on Activated Rh-Doped Pd. *J. Am. Chem. Soc.* **2024**, *146* (12), 8641–8649. https://doi.org/10.1021/jacs.4c00312.

(16) Ke, J.; Zhao, J.; Chi, M.; Wang, M.; Kong, X.; Chang, Q.; Zhou, W.; Long, C.; Zeng, J.; Geng, Z. Facet-Dependent Electrooxidation of Propylene into Propylene Oxide over Ag_3PO_4 Crystals. *Nat. Commun.* **2022**, *13* (1), 932. https://doi.org/10.1038/s41467-022-28516-0.

(17) Koroidov, S.; Winiwarter, A.; Diaz-Morales, O.; Görlin, M.; Halldin Stenlid, J.; Wang, H. Y.; Börner, M.; Goodwin, C. M.; Soldemo, M.; Pettersson, L. G. M.; Rossmeisl, J.; Hansson, T.; Chorkendorff, I.; Nilsson, A. Chemisorbed Oxygen or Surface Oxides Steer the Selectivity in Pd Electrocatalytic Propene Oxidation Observed ByoperandoPd L-Edge X-Ray Absorption Spectroscopy. *Catal. Sci. Technol.* **2021**, *11* (10), 3347–3352. https://doi.org/10.1039/d0cy02134b.

(18) Winiwarter, A.; Boyd, M. J.; Scott, S. B.; Higgins, D. C.; Seger, B.; Chorkendorff, I.; Jaramillo, T. F. CO as a Probe Molecule to Study Surface Adsorbates during Electrochemical Oxidation of Propene. *ChemElectroChem* **2021**, *8* (1), 250–256. https://doi.org/10.1002/celc.202001162.

(19) Iguchi, S.; Kataoka, M.; Hoshino, R.; Yamanaka, I. Direct Epoxidation of Propylene with Water at a PtO_x Anode Using a Solid-Polymer-Electrolyte Electrolysis Cell. *Catal. Sci. Technol.* **2022**, *12* (2), 469–473. https://doi.org/10.1039/d1cy01888d.

(20) Otsuka, K.; Ushiyam, T.; Yamanaka, I.; Ebitani, K. Electrocatalytic Synthesis of Propylene Oxide during Water Electrolysis. *J. Catal.* **1995**, *157*, 450–460.

(21) De Luna, P.; Hahn, C.; Higgins, D.; Jaffer, S. A.; Jaramillo, T. F.; Sargent, E. H. What Would It Take for Renewably Powered Electrosynthesis to Displace Petrochemical Processes? *Science* **2019**, *364* (6438), eaav3506. https://doi.org/10.1126/science.aav3506.

(22) Trent, D. L. Propylene Oxide. In *Kirk-Othmer Encyclopedia of Chemical Technology*; Wiley, 2001. https://doi.org/10.1002/0471238961.1618151620180514.a01.pub2.

(23) Nijhuis, T. A.; Makkee, M.; Moulijn, J. A.; Weckhuysen, B. M. The Production of Propene Oxide: Catalytic Processes and Recent Developments. *Ind. Eng. Chem. Res.* **2006**, *45* (10), 3447–3459. https://doi.org/10.1021/ie0513090.

(24) Zhang, P.; Wang, T.; Gong, J. Advances in Electrochemical Oxidation of Olefins to Epoxides. *CCS Chem.* **2023**, *5* (5), 1028–1042. https://doi.org/10.31635/ccschem.023.202202643.

(25) Khatib, S. J.; Oyama, S. T. Direct Oxidation of Propylene to Propylene Oxide with Molecular Oxygen: A Review. *Catal. Rev.* **2015**, *57* (3), 306–344. https://doi.org/10.1080/01614940.2015.1041849.

(26) Leow, W. R.; Lum, Y.; Ozden, A.; Wang, Y.; Nam, D.-H.; Chen, B.; Wicks, J.; Zhuang, T.-T.; Li, F.; Sinton, D.; Sargent, E. H. Chloride-Mediated Selective Electrosynthesis of Ethylene and Propylene Oxides at High Current Density. *Science* **2020**, *368* (6496), 1228–1233. https://doi.org/10.1126/science.aaz8459.

(27) Wang, J.; Dong, X.; Feng, G.; Lu, X.; Wu, G.; Li, G.; Li, S.; Mao, J.; Chen, A.; Song, Y.; Zeng, J.; Wei, W.; Chen, W. Spatial-coupled Ampere-level Electrochemical Propylene Epoxidation over RuO_2/Ti Hollow-fiber Penetration Electrodes. *Angew. Chem. Int. Ed.* **2024**, e202411173. https://doi.org/10.1002/anie.202411173.

(28) Sauvé, E. R.; Tang, B. Y.; Razdan, N. K.; Toh, W. L.; Weng, S.; Surendranath, Y. Open Circuit Potential Decay Transients Quantify Interfacial PH Swings during High Current Density Hydrogen Electrocatalysis. *Joule* **2024**, *8* (3), 728–745. https://doi.org/10.1016/j.joule.2024.01.004.

(29) Wang, Y.; Ren, J.; Deng, K.; Gui, L.; Tang, Y. Preparation of Tractable Platinum, Rhodium, and Ruthenium Nanoclusters with Small Particle Size in Organic Media. *Chem. Mater.* **2000**, *12* (6), 1622–1627. https://doi.org/10.1021/cm0000853.

(30) Bonet, F.; Delmas, V.; Grugeon, S.; Herrera Urbina, R.; Silvert, P.-Y.; Tekaia-Elhsissen, K. Synthesis of Monodisperse Au, Pt, Pd, Ru and Ir Nanoparticles in Ethylene Glycol. *Nanostruct. Mater.* **1999**, *11* (8), 1277–1284. https://doi.org/10.1016/S0965-9773(99)00419-5.

(31) Bock, C.; Paquet, C.; Couillard, M.; Botton, G. A.; MacDougall, B. R. Size-Selected Synthesis of PtRu Nano-Catalysts: Reaction and Size Control Mechanism. *J. Am. Chem. Soc.* **2004**, *126* (25), 8028–8037. https://doi.org/10.1021/ja0495819.

(32) Hoshi, N.; Kagaya, K.; Hori, Y. Voltammograms of the Single-Crystal Electrodes of Palladium in Aqueous Sulfuric Acid Electrolyte: Pd(S)-[n(111)×(111)] and Pd(S)-[n(100)×(111)]. *J. Electroanal. Chem.* **2000**, *485* (1), 55–60. https://doi.org/10.1016/S0022-0728(00)00098-X.

(33) Hoshi, N.; Kuroda, M.; Hori, Y. Voltammograms of Stepped and Kinked Stepped Surfaces of Palladium: Pd(S)-[n(111)×(100)] and Pd(S)-[n(100)×(110)]. *J. Electroanal. Chem.* **2002**, *521* (1–2), 155–160. https://doi.org/10.1016/S0022-0728(02)00687-3.

(34) Hara, M.; Linke, U.; Wandlowski, T. Preparation and Electrochemical Characterization of Palladium Single Crystal Electrodes in 0.1 M H_2SO_4 and $HClO_4$. Part I. Low-Index Phases. *Electrochim. Acta* **2007**, *52* (18), 5733–5748. https://doi.org/10.1016/j.electacta.2006.11.048.

(35) Grdeń, M.; Łukaszewski, M.; Jerkiewicz, G.; Czerwiński, A. Electrochemical Behaviour of Palladium Electrode: Oxidation, Electrodissolution and Ionic Adsorption. *Electrochim. Acta*. November 1, 2008, pp 7583–7598. https://doi.org/10.1016/j.electacta.2008.05.046.

(36) Stevens, D. A.; Dahn, J. R. Electrochemical Characterization of the Active Surface in Carbon-Supported Platinum Electrocatalysts for PEM Fuel Cells. *J. Electrochem. Soc.* **2003**, *150* (6), A770. https://doi.org/10.1149/1.1573195.

(37) Daubinger, P.; Kieninger, J.; Unmüssig, T.; Urban, G. A. Electrochemical Characteristics of Nanostructured Platinum Electrodes-A Cyclic Voltammetry Study. *Phys. Chem. Chem. Phys.* **2014**, *16* (18), 8392–8399. https://doi.org/10.1039/c4cp00342j.

(38) Stoerzinger, K. A.; Qiao, L.; Biegalski, M. D.; Shao-Horn, Y. Orientation-Dependent Oxygen Evolution Activities of Rutile IrO_2 and RuO_2. *J. Phys. Chem. Lett.* **2014**, *5* (10), 1636–1641. https://doi.org/10.1021/jz500610u.

(39) Kuo, D.-Y.; Kawasaki, J. K.; Nelson, J. N.; Kloppenburg, J.; Hautier, G.; Shen, K. M.; Schlom, D. G.; Suntivich, J. Influence of Surface Adsorption on the Oxygen Evolution Reaction on IrO_2 (110). *J. Am. Chem. Soc.* **2017**, *139* (9), 3473–3479. https://doi.org/10.1021/jacs.6b11932.

(40) Geppert, J.; Röse, P.; Czioska, S.; Escalera-López, D.; Boubnov, A.; Saraçi, E.; Cherevko, S.; Grunwaldt, J.-D.; Krewer, U. Microkinetic Analysis of the Oxygen Evolution Performance at Different Stages of Iridium Oxide Degradation. *J. Am. Chem. Soc.* **2022**, *144* (29), 13205–13217. https://doi.org/10.1021/jacs.2c03561.

(41) Abild-Pedersen, F.; Greeley, J.; Studt, F.; Rossmeisl, J.; Munter, T. R.; Moses, P. G.; Skúlason, E.; Bligaard, T.; Nørskov, J. K. Scaling Properties of Adsorption Energies for Hydrogen-Containing Molecules on Transition-Metal Surfaces. *Phys. Rev. Lett.* **2007**, *99* (1), 016105. https://doi.org/10.1103/PhysRevLett.99.016105.

(42) Kuo, D.-Y.; Paik, H.; Kloppenburg, J.; Faeth, B.; Shen, K. M.; Schlom, D. G.; Hautier, G.; Suntivich, J. Measurements of Oxygen Electroadsorption Energies and Oxygen Evolution Reaction on RuO_2 (110): A Discussion of the Sabatier Principle and Its Role in Electrocatalysis. *J. Am. Chem. Soc.* **2018**, *140* (50), 17597–17605. https://doi.org/10.1021/jacs.8b09657.

(43) Zhang, H.; Chen, B.; Liu, T.; Brudvig, G. W.; Wang, D.; Waegele, M. M. Infrared Spectroscopic

Observation of Oxo- and Superoxo-Intermediates in the Water Oxidation Cycle of a Molecular Ir Catalyst. *J. Am. Chem. Soc.* **2024**, *146* (1), 878–883. https://doi.org/10.1021/jacs.3c11206.

(44) Hong, W. T.; Risch, M.; Stoerzinger, K. A.; Grimaud, A.; Suntivich, J.; Shao-Horn, Y. Toward the Rational Design of Non-Precious Transition Metal Oxides for Oxygen Electrocatalysis. *Energy Environ. Sci.* **2015**, *8* (5), 1404–1427. https://doi.org/10.1039/C4EE03869J.

(45) Man, I. C.; Su, H.; Calle-Vallejo, F.; Hansen, H. A.; Martínez, J. I.; Inoglu, N. G.; Kitchin, J.; Jaramillo, T. F.; Nørskov, J. K.; Rossmeisl, J. Universality in Oxygen Evolution Electrocatalysis on Oxide Surfaces. *ChemCatChem* **2011**, *3* (7), 1159–1165. https://doi.org/10.1002/cctc.201000397.

(46) Morales, D. M.; Risch, M. Seven Steps to Reliable Cyclic Voltammetry Measurements for the Determination of Double Layer Capacitance. *J. Phys. Energy* **2021**, *3* (3), 034013. https://doi.org/10.1088/2515-7655/abee33.

(47) de Veij, M.; Vandenabeele, P.; De Beer, T.; Remon, J. P.; Moens, L. Reference Database of Raman Spectra of Pharmaceutical Excipients. *J. Raman Spectros.* **2009**, *40* (3), 297–307. https://doi.org/10.1002/jrs.2125.

(48) Krishnan, K.; Krishnan, R. S. Raman and Infrared Spectra of Ethylene Glycol. *Proceedings of the Indian Academy of Sciences - Section A* **1966**, *64* (2), 111. https://doi.org/10.1007/BF03047675.

(49) Sawodny, W.; Niedenzu, K.; Dawson, J. W. The Vibrational Spectrum of Ethylene Glycol. *Spectrochim. Acta A* **1967**, *23* (4), 799–806. https://doi.org/10.1016/0584-8539(67)80007-2.

(50) Smith, B. C. The Infrared Spectra of Polymers V: Epoxies. *Spectroscopy* **2022**, 17–19. https://doi.org/10.56530/spectroscopy.mg2473z4.

(51) Johnson, R. D. III. Experimental data for C_3H_6O (Propylene oxide). *NIST Standard Reference Database.* https://cccbdb.nist.gov/exp2x.asp?casno=75569&charge=0

(52) Serra, M. C. C.; da Fonseca, M. M. R.; Calado, J. C. G.; Palavra, A. M. F. Solubility of Propene in Water and in a Mineral Medium for the Cultivation of a XanthobacterStrain. *J. Solution Chem.* **1998**, *27* (5), 455–461. https://doi.org/10.1023/A:1022604705859.

(53) Kolen, M.; Ripepi, D.; Smith, W. A.; Burdyny, T.; Mulder, F. M. Overcoming Nitrogen Reduction to Ammonia Detection Challenges: The Case for Leapfrogging to Gas Diffusion Electrode Platforms. *ACS Catal.* **2022**, *12* (10), 5726–5735. https://doi.org/10.1021/acscatal.2c00888.

(54) Koper, M. T. M. Analysis of Electrocatalytic Reaction Schemes: Distinction between Rate-Determining and Potential-Determining Steps. *J. Solid State Electrochem.* **2013**, *17* (2), 339–344. https://doi.org/10.1007/s10008-012-1918-x.

(55) Guilherme Buzanich, A.; Radtke, M.; Yusenko, K. V.; M. Stawski, T.; Kulow, A.; Cakir, C. T.; Röder, B.; Naese, C.; Britzke, R.; Sintschuk, M.; Emmerling, F. BAM *Line* —A Real-Life Sample Materials Research Beamline. *J. Chem. Phys.* **2023**, *158* (24), 244202. https://doi.org/10.1063/5.0157194.